Anal Bioanal Chem
DOI 10.1007/s00216-013-7233-2

RESEARCH PAPER

Refining the statistical model for quantitative immunostaining of surface-functionalized nanoparticles by AFM

Robert I. MacCuspie · Danielle E. Gorka

Received: 12 April 2013 / Revised: 11 June 2013 / Accepted: 9 July 2013

Abstract Recently, an atomic force microscopy (AFM)-based approach for quantifying the number of biological molecules conjugated to a nanoparticle surface at low number densities was reported. The number of target molecules conjugated to the analyte nanoparticle can be determined with single nanoparticle fidelity using antibody-mediated self-assembly to decorate the analyte nanoparticles with probe nanoparticles (i.e., quantitative immunostaining). This work refines the statistical models used to quantitatively interpret the observations when AFM is used to image the resulting structures. The refinements add terms to the previous statistical models to account for the physical sizes of the analyte nanoparticles, conjugated molecules, antibodies, and probe nanoparticles. Thus, a more physically realistic statistical computation can be implemented for a given sample of known qualitative composition, using the software scripts provided. Example AFM data sets, using horseradish peroxidase conjugated to gold nanoparticles, are presented to illustrate how to implement this method successfully.

Keywords Gold nanoparticles · Atomic force microscopy · Quantitative immunostaining · Functionalized AuNPs

Introduction

Surface-functionalized nanoparticles (NPs) have seen increasing applications in recent years, for example, as multifunctional nanomedicine platforms with both targeting and therapeutic conjugates [1–3]. However, to both successfully commercialize these materials and perform robust structure–property studies, quantifying the number of ligands per NP is critical [4, 5]. This is especially true in regulated fields such as nanomedicine clinical trials [6, 7]. Many integrative techniques (i.e., all NPs are measured and average values reported) are currently employed, such as digestion coupled with chemical analysis [7–12], X-ray photoelectron spectroscopy [13], dynamic light scattering (DLS) plus infrared spectroscopy [14], or advanced nuclear magnetic resonance spectroscopy [15, 16]. Combinations of physical size measurements can inform on the average degree of surface molecule adsorption as well as conformation [17]. However, integrative techniques by definition cannot inform on whether there is a heterogeneous distribution of coating densities on the collection of NPs assayed. It has been reported that attempts to stoichiometrically control the surface-functionalization of NPs leads to heterogeneous distributions [18]. Fluorescence techniques could use either direct labeling of proteins with fluorescent molecules onto reactive sites on the proteins or fluorescently tagged antibodies. However, such fluorescence techniques only provide an integrative measurement of the average number of target proteins bound per nanoparticle, by measuring the fluorescence increase after tagging all proteins in the solution. The ability to measure whether a distribution of stoichiometries result in NP surface functionalization remains a challenge for integrative techniques.

Electronic supplementary material The online version of this article (doi:10.1007/s00216-013-7233-2) contains supplementary material, which is available to authorized users.

R. I. MacCuspie (✉) · D. E. Gorka
Materials Measurements Science Division, Material Measurement Laboratory, National Institute of Standards and Technology, Gaithersburg, MD 20899, USA
e-mail: robert.maccuspie@nist.gov

Present Address:
R. I. MacCuspie
Nanotechnology and Multifunctional Materials Program, Florida Polytechnic University, Lakeland, FL 33801, USA
e-mail: rmaccuspie@floridapolytechnic.org

Present Address:
D. E. Gorka
Department of Chemistry, Duke University, Durham, NC 27708, USA

Published online: 31 July 2013

Microscopy techniques, such as transmission electron microscopy (TEM) and atomic force microscopy (AFM), are capable of imaging single NPs and thus can overcome the limitations of integrative techniques. Within microscopy communities, immunostaining approaches have been used for decades to qualitatively identify the presence and location of biomolecules (often within cells) and to semi-quantitatively assay for the concentration of their expression in cellular systems. Historically, immunostaining has been dominated by fluorescently tagged antibodies combined with light microscopy [19, 20], and gold nanoparticle (AuNP) tagged antibodies combined with TEM [21–23]. Extending immunostaining into semi-quantitative or quantitative measurements has also been reported [24, 25]. Recently, probe antibody-NPs were demonstrated to be quantitative in measuring the number of biomolecules conjugated to the surfaces of analyte NPs, with single NP resolution when combined with AFM imaging [26]. Previously described as self-limiting self-assembly, this work will henceforth be referred to as quantitative immunostaining by AFM.

Quantitative interpretation of immunostaining AFM images is a recent development [26]. Figure 1 illustrates the overall scheme for implementation of quantitative immunostaining. In quantitative immunostaining by AFM, small-diameter "probe" nanoparticles tagged with antibodies are used to decorate the surface of a protein-functionalized larger-diameter "analyte" nanoparticle. The antibodies on the probe nanoparticles are able to specifically recognize the proteins on the analyte nanoparticle and thus self-assemble into a raspberry-like structure, where each small probe nanoparticle that binds aids in visualizing one of the proteins bound to the surface of the analyte nanoparticle. AFM provides the opportunity to automate much of the data collection process at lower initial instrument infrastructure costs when compared with TEM [27, 28]. Additionally, recent advances have demonstrated how to analyze AFM data in an automated fashion [29]. However, quantitatively interpreting an AFM topography image of a biomolecule-conjugated AuNP is challenging due to topographic measurements only imaging the "top half" of the structures. Additionally, because of steric considerations, the number of probe NPs assembled onto the analyte NP is often less than the number of biomolecules conjugated to the surface of the analyte NP. A statistical model must be used to relate the observed data back to probabilities of physically possible combinations. A previously reported model [26] was a good first approximation of the statistical probabilities involved for topographic images, with numerous assumptions that made calculating results easily tractable. This work aims to refine that existing model by explicitly analyzing every physically possible geometric combination, including terms to account for the physical sizes of each NP (analyte and probe), conjugated biomolecule, and probe antibody. Software routines are presented that enable this more physically realistic interpretation of the data. Additionally, this work will also provide examples of how to successfully implement the model when interpreting example data sets.

Experimental[1]

Figure 1 illustrates the overall scheme for implementation of quantitative immunostaining. A simplified protocol can be found at the end of the experimental section.

Synthesis of functionalized AuNPs

Synthesis followed previously reported procedures [26], using nominally 10-, 30-, and 60-nm diameter AuNPs (Part numbers 15703–1, 15706–1, 15708–6, respectively, Ted Pella, Redding,CA), horseradish peroxidase (HRP) (#01-2001, Life Technologies, Grand Island, NY), and anti-HRP antibody (#ab34580, AbCam, Cambridge, MA), and are detailed in the Electronic supplementary material. N_{Lig} will describe the stoichiometry of the number of ligands per analyte NP, i.e., the number of HRP molecules per AuNP. Fig. S1 (Electronic supplementary material) illustrates the synthesis approach. Fig. S2 (Electronic supplementary material) shows typical characterization data for reaction products.

Sample prep and AFM imaging

A tenfold molar excess of probe NPs (10 nm AuNPs functionalized with a single anti-HRP antibody, sometimes called Ab-AuNPs) were added to the analyte NPs (30 or 60 nm AuNPs functionalized with multiple HRP molecules) and allowed to react for 1 h. A 20 μL droplet of the solution was then placed over an amine-functionalized Si chip (prepared as described by NIST-NCL PCC-7) for either 10 min for 30 nm AuNPs, or 30 min for 60 nm AuNPs, then rinsed with deionized water and dried with short blasts of filtered compressed air. No less than 20 locations around a substrate were imaged using a Bruker Dimension 3100 AFM (Santa Barbara, CA). A programmed move was used to collect up to 100 images in one session. AFM tips (Tap150Al-G, NanoAndMore, Lady Island, SC) were discarded after each session.

[1] Certain trade names and company products are mentioned in the text or identified in illustrations in order to specify adequately the experimental procedure and equipment used. In no case does such identification imply recommendation or endorsement by National Institute of Standards and Technology, nor does it imply that the products are necessarily the best available for the purpose.

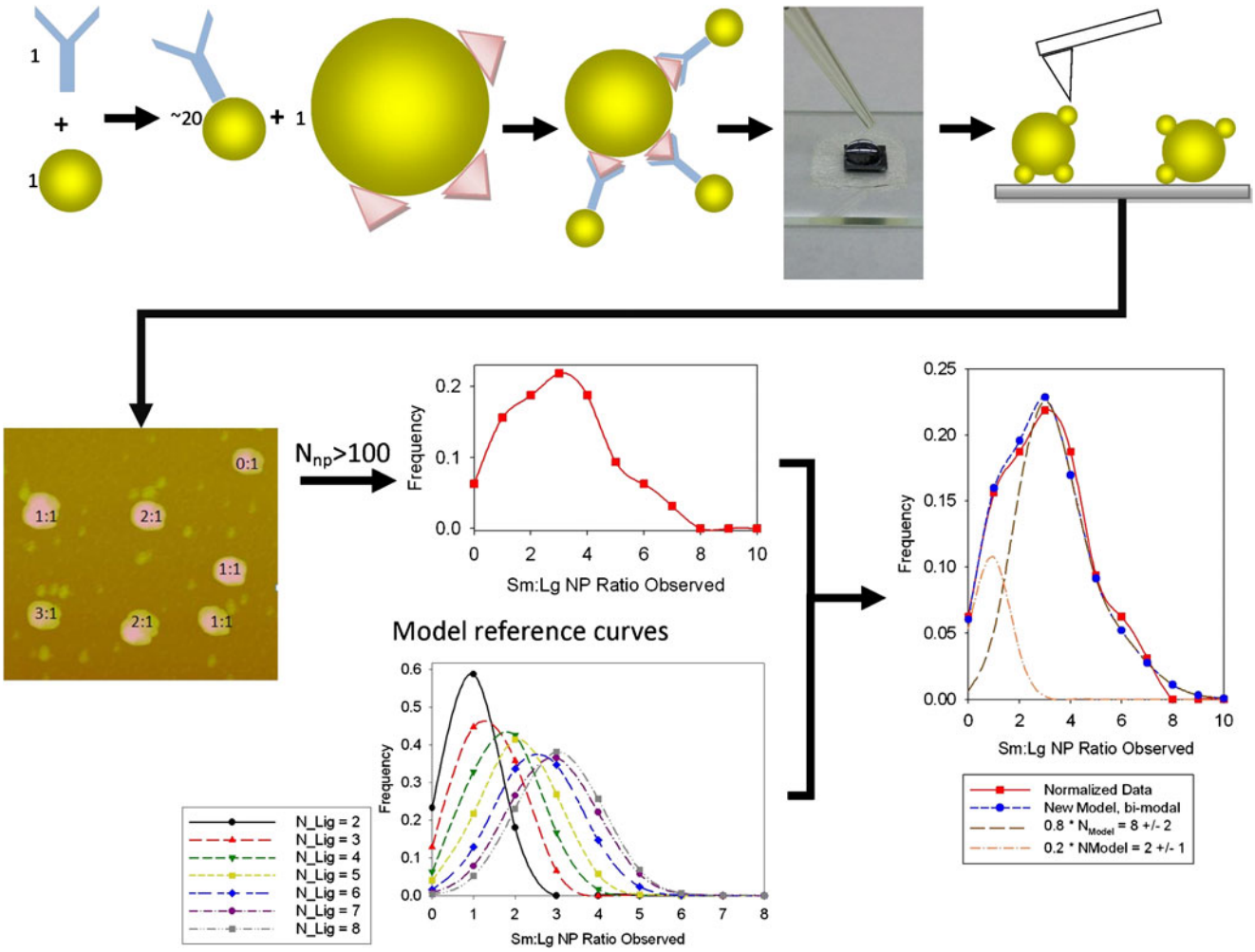

Fig. 1 Representation of quantitative immunostaining procedure

AFM data analysis

For each 5×5-μm AFM image, probe NP+analyte NP assemblies were visually identified. Examples of images obtained can be found in Fig. S3 (Electronic supplementary material). Only assemblies with appropriately sized smaller probe NPs and one large analyte NP were included for analysis. When analyzing the data, a 20 nm distance cutoff was considered. This upper bound summed the size of the HRP molecule (approximately 4.5 nm in diameter [30]), the IgG antibody molecule (approximately 14 nm in diameter [31]), and an additional 1.5 nm to approximate an extended conformation of the molecules linking the HRP or IgG antibody biomolecules to their respective NPs, such as the assemblies illustrated in Figs. 1 and 2. It was assumed all probe NPs had one antibody per NP, thereby preventing formation of massive networks such as those seen with peptide nanotube biosensors [32]. Thus, infrequently occurring agglomerates of large analyte NPs were not counted due to this ambiguity in quantitative interpretation. Analysis of a greater number of assemblies will lead to a greater degree of confidence in the data analysis; just as when collecting diameter measurements of nanoparticles, $N>100$ is an absolute minimum, with $N>300$ preferred when possible.

Statistical model for quantitative interpretation of AFM data

The predictions of the number of probe NPs per analyte NP were calculated explicitly for each possible combination of ligand positions using a MATLAB code "ReferenceCodeGenerator.m" (see Electronic supplementary material). First, a reference curve with a mean of N_{Lig} HRP molecules per analyte NP and a standard deviation of 0 was calculated. The total number of possible ligand binding sites on the analyte NP, N_{BS}, is determined by dividing the surface area of the analyte NP by the cross-sectional area of the ligand and rounding to the nearest integer,

$$N_{\mathrm{BS}} = \frac{4\pi r_{\mathrm{analyteNP}^2}}{\pi r_{\mathrm{Lig}^2}} \quad (1)$$

where $r_{\mathrm{analyteNP}}$ is the radius of the analyte NP and r_{Lig} is the

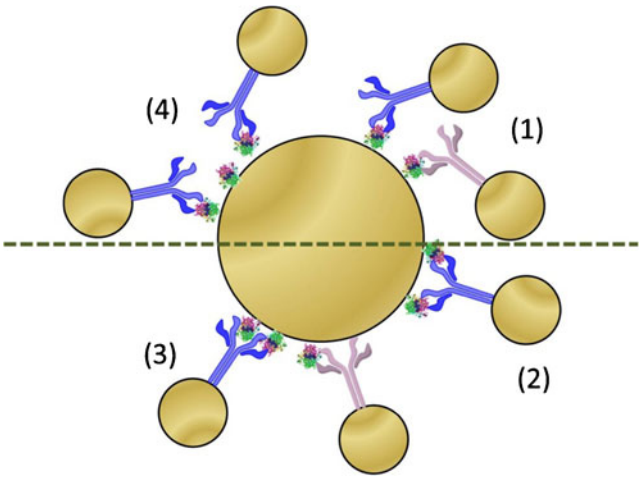

Fig. 2 Illustration of challenges for successful execution of quantitative AFM immunostaining, to scale for 30 nm core AuNP, 4.5 nm HRP enzyme, 10 nm probe AuNP, and 11 nm IgG antibody. *Clockwise from upper right*, (*1*) polyclonal antibodies (represented by *different colors*) reduce false-negatives from HRP orientation distributions; (*2*) IgG molecules can potentially bind two HRP molecules; the physical size of the Ab-AuNP can sterically block HRP molecules, either (*3*) by one Ab-AuNP or (*4*) by multiple Ab-AuNPs in close proximity. Finally, it must be assumed that only those antibody-AuNPs on the *top half of the figure* (*above the green dashed line*) will be imaged by a topographic technique such as AFM

radius of the ligand molecule. For simplicity, binding sites were assigned sequential integers as "position coordinates." Next, a so-called position matrix was built such that there were N_{Lig} columns and one row for each possible combination of binding site locations; for example, a position matrix with N_{Lig}=3 and 100 possible binding sites would have 100×99×98, or 970,200 rows. Each row contained a unique combination of position coordinates representing where each of the N_{Lig} ligands attached (i.e., where each HRP molecule attached onto the analyte NP surface). Next, a so-called binding matrix was built, with an identical number of rows and columns as the position matrix. The binding matrix was used to analyze how many probe NPs would be able to bind the surface of the hypothetical analyte NP's prescribed geometry. Initially, the binding matrix was completely populated with zeros, to represent the state before the probe NPs were mixed with the analyte NPs. The binding matrix was analyzed one row at a time, for each ligand position. As each row was analyzed, the first ligand position would always have an antibody attached. For each subsequent position, the algorithm would look backwards and calculate the distance between the current ligand position and the previous ligand positions in the binding matrix. To account for the antibody's larger size physically blocking ligands located nearby each other on the surface, the number of blocked binding sites, q, was calculated by dividing the cross-sectional area of the antibody by the cross-sectional area of the ligand and rounding up to the next integer,

$$q = \frac{\pi r_{\text{Antibody}^2}}{\pi r_{\text{Lig}^2}} \tag{2}$$

where r_{Antibody} is the radius of the antibody. If the distance between ligands was less than q, a probe NP was allowed to bind to the current position, p, in the binding matrix only if no probe NP was bound in the previous position(s); if probe NP was already bound to a position within q binding sites of p, the binding matrix value remained zero to represent the case of being sterically blocked.

After completing the binding matrix, the number of probe NPs that would be visualized by AFM was determined. For a given row of the binding matrix, only the values for positions that correspond to the first half of possible binding sites (i.e., if $p \leq N_{BS}/2$ in the binding matrix) were counted; the results were then normalized to be a set of probabilities. The probabilities represent the number of probe NPs predicted to be visualized by a topographic measurement, such as AFM, for the given geometric configuration of ligand attachment to the analyte NP, assuming all analyte NPs contained exactly N_{Lig} molecules.

To incorporate a standard deviation about the mean of N_{Lig}, the nomenclature for monomodal fits will follow a $N_{model}=X\pm Y$ format, where X represents the mean number of HRP ligands per analyte NP and Y represents the number of standard deviations about the mean, and thus the width of the distribution. A table was developed to add the fractional contribution of each mean curve with a standard deviation of 0 to the final $N_{model}=X\pm Y$ reference curve. See Table S1, Electronic supplementary material for additional details.

Fits to the data can be performed empirically in a spreadsheet, or by using the software scripts "FitQIdata3.m" to analyze a single dataset or "FitLotsOData.m" to analyze multiple datasets. To compare how close various model fits are, the term "residual" is defined in this work as the sum of the absolute values of differences between the model and data overall histogram points. Due to the fact all model and data histograms were normalized to integrate to 1, the maximum possible residual value is 2.

For bimodal distributions, the percent weighting given to each component will be listed in the format Q % $N_{model}=X_1\pm Y_1$, R % $N_{model}=X_2\pm Y_2$. The "fit mean" term is used for the overall weighted average, while the "standard deviation" is the square root of the weighted sum of the squares of the differences between the components of the model and the mean of the model.

The overall procedure can be summarized in the simplified protocol presented below and illustrated in the scheme in Fig. 1.

Simplified protocol

1. Fabricate probe NPs (covalently attach antibodies to small (e.g., 10 nm) NPs).
2. Add a tenfold excess number of probe NPs to the analyte NPs.
3. Incubate at room temperature for 1 h, or at 4 °C for 24 h.
4. Place a 20 μL droplet onto an aminosilane-functionalized silicon wafer chip (e.g., 5 by 5 mm) at room temperature for 10 to 30 min.
5. Rinse wafer chip with filtered DI water; dry with compressed filtered air.
6. Collect AFM images from multiple locations on chip.
7. Identify the probe/analyte NP ratio for each assembly imaged.
8. Create a histogram from $N>100$ assemblies.
9. Generate SD=0 reference curve data using MATLAB script "ReferenceCurveGenerator.m," entering in parameters for diameters of antibodies and ligand proteins and number of ligands in lines of code 6–10 and commenting out 'for' loops appropriately in lines 29–49 and 59–81 (see Electronic supplementary material).
10. Generate SD=X (X=1, 2, etc.) reference curve data using the Excel spreadsheet approach identified in the Electronic supplementary material.
11. Fit reference curves to data using MATLAB script "FitQIdata3.m" for a single column of data, or "FitLostOData.m" for many data sets (see Electronic supplementary material).

Results and discussion

Figure 2 illustrates some of the challenges to quantitative interpretation of AFM immunostaining results and how they can be overcome. Specifically: (1) epitope orientation with respect to the surface is likely a distribution, thereby reducing the number of times monoclonal antibodies would recognize the analyte biomolecules; (2) IgG molecules can bind up to two analyte molecules; (3) the IgG molecule is often much larger than the analyte molecule, thereby potentially physically or sterically blocking other HRP molecules from binding antibodies; and (4) when several target molecules are in close physical proximity to one another on the analyte NP surface, the first probe NP in close proximity could potentially sterically hinder a precise 1:1 binding of subsequent probe NPs to analyte molecules.

The model in this work overcomes these challenges by making three previously reported assumptions [26] (1–3), and two new ones (4–5): (1) an HRP analyte molecule will attach with a random distribution of locations on the analyte NP surface, (2) the self-assembled probe NP+analyte NP structures deposit onto the AFM substrates with random orientations, (3) only half of the bound probe NPs will be imaged as AFM is a topographic technique, (4) at least one epitope is always oriented away from the analyte NP surface and thus available for antibody binding by the probe NP, and (5) the physically larger size of an antibody could sterically block multiple ligand molecules in close proximity on the analyte NP surface from each being recognized by one antibody each.

The two new assumptions, (4) and (5), are added to address the previously ignored challenges. Assumption (4) addresses challenge (1) through the use of polyclonal antibodies. A random molecular orientation of HRP molecules relative to the analyte NP surface can be accommodated by using polyclonal antibodies since it is more likely an antibody will find an epitope on the HRP molecule that is "face up" if there are multiple epitopes that can be recognized. Assumption (5) addresses challenges 2–4, because each of these mechanisms can be treated identically mathematically. Each HRP molecule is assigned a position coordinate on the surface of the analyte AuNP. As the antibody binding matrix is analyzed, the position coordinates of the previous q spaces are examined, where q represents the number of binding sites sterically blocked by challenges 2–4. Only if all q neighboring spaces are "empty" (i.e., 0) will the HRP molecule position be populated in the binding matrix as having a probe NP bound (i.e., 1). By explicitly solving for all possible combinations of position coordinates, a series of reference probability curves was created.

Example reference curves are provided in Fig. 3a for 30 nm analyte NPs for N_{model} ranging from (2±1) to (8±1) HRP ligands per analyte NP. It is interesting to note that the average value for the new models increase less rapidly than a Pascal's triangle model does (Fig. 3b). This is increasing deviation between the naive statistics ,and the more physically realistic models is due to the increasing probability that one or more HRP molecules will not be recognized by a probe NP, for all of the challenges identified previously. It is speculated that the slope of such plots could be used in the future to determine the suitability of detection response for a given combination of analyte NP, ligand molecule, and probe NP sizes and perhaps predict the upper bound for measuring N_{Lig} by quantitative immunostaining.

The role of the ligand size to the nanoparticle size is examined in Fig. 3c. Reference distribution curves for a range of analyte NP diameters from 15 to 60 nm were calculated for N_{model}=5±0 HRP ligands per analyte NP. As the analyte NP diameter increases, so does the likely space between the ligands on the surface. This space in turn leads to a greater likelihood that all ligands on the surface will be recognized by one probe NP, as evidenced by the reference curve for a 60 nm analyte NP approaching the Pascal's triangle probability. Recognizing the challenges of intercomparing sizing results of NPs [33, 34] and

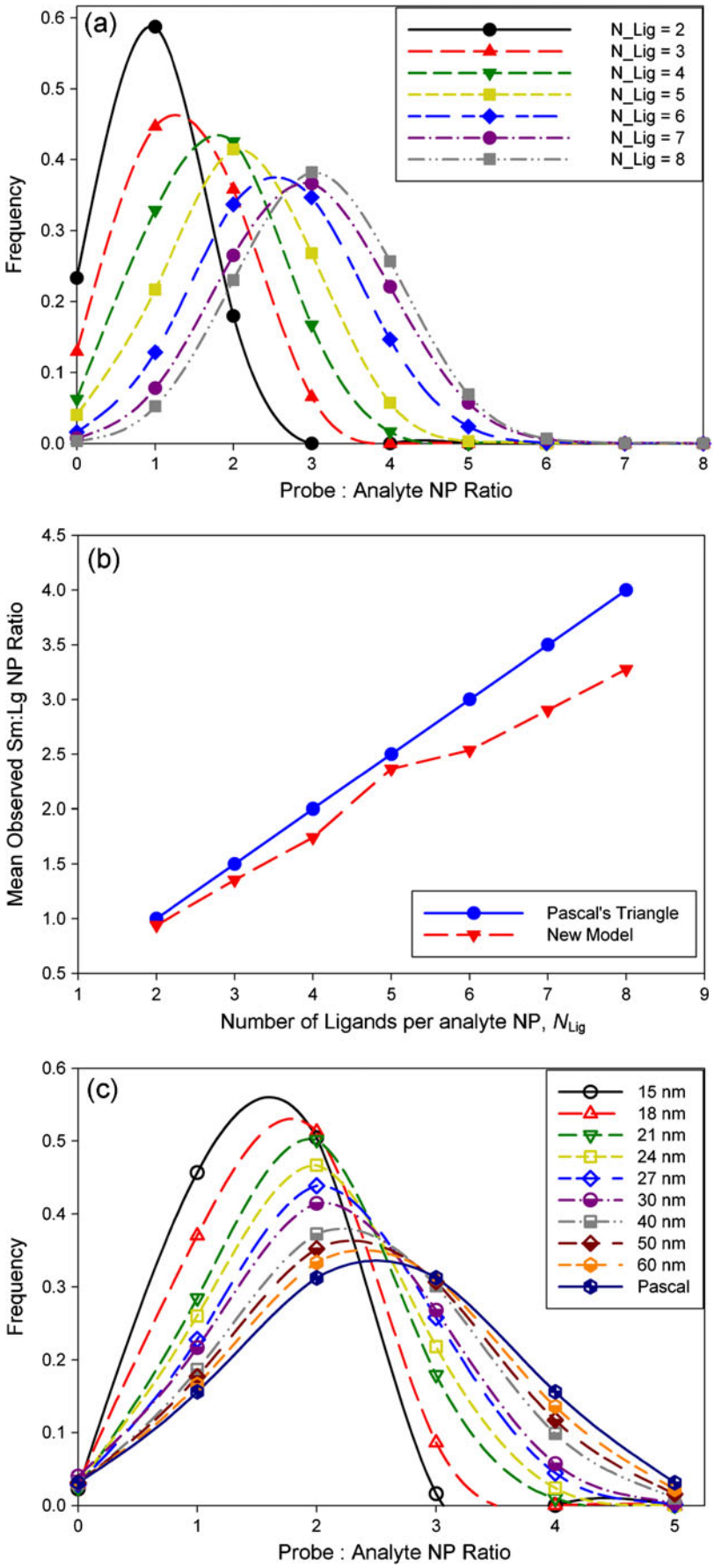

Fig. 3 **a** Model distributions for 30 nm analyte NP for $N_{Lig}=2\pm1$ to $N_{Lig}=8\pm1$ ligands 4.5 nm diameter, and IgG molecules were assumed to be 14 nm diameter. **b** Integrated average from 2-D coarse-grained model of HRP ligands on a 30 nm analyte NP, compared with the Pascal's triangle average probability. **c** Role of physical size ratio of analyte NPs and ligands. Distributions for analyte NPs of varying diameters with $N_{Lig}=5\pm0$ for ligands 6 nm in diameter

the propensity of NPs to agglomerate in biological media [35–37], the authors recommend using a measured diameter of the analyte NPs for AuNPs based upon the metallic Au core diameter (such as from AFM, TEM, or small-angle X-ray scattering), as opposed to a hydrodynamic diameter (such as from DLS or nanoparticle tracking analysis), when inputting the analyte NP diameter into the statistics calculations.

Having now gained an understanding that it is best to calculate the reference curves for the given analyte NP, ligand, and probe NP diameters in the system being analyzed, a few brief examples will be provided on how to interpret actual results. First, previously reported data [26] is re-analyzed, and a comparison of the old and new models for data on 60 nm Au analyte NPs with N_{Lig}=10 is shown in Fig. 4a. By combining a weighted average of two reference curves (80 % N_{model}=8±2, 20 % N_{model}=2±1), the residual drops from 0.52 for the old monomodal model to 0.07 for the new bimodal model. The fit mean value of ligands bound per analyte NP predicted by the new model also increases to 6.8, from 6.0 using the old model, in closer agreement with the theoretical yield of this reaction's stoichiometry.

New datasets were also collected as examples. Here, analyte NPs were fabricated by conjugating HRP to either 30 nm (Fig. 4b–c) or 60 nm (Fig. 5) diameter AuNPs (HRP-AuNPs) in a variety of solution stoichiometries. Figures 4b–c analyze the products from two separate synthesis batches of 30 nm HRP-AuNPs with N_{Lig}=10. In the first batch (Fig. 4b), N_{model}=7±2 fits the data well with a residual of 0.13. However, in the second batch (Fig. 4c), a weighted average of two models fits the data better, 30 % N_{model}=7±1, 70 % N_{model}=9±1, with a residual of 0.15. This bi-modal model yields a lower residual compared with either the mono-modal N_{model}=8±1 or the mono-modal N_{model}=9±1 models shown as dashed lines.

Figure 5 shows a series of 60 nm HRP-AuNPs with N_{Lig}=5, 7, and 12, respectively. A bi-modal distribution fit provided reasonably low residuals in each case. For N_{Lig}=5 (Fig. 5a), 60 % N_{model}=2±1, 40 % N_{model}=5±1 yielded a residual of 0.22 and a fit mean of 3.2. For N_{Lig}=7 (Fig. 5b), 50 % N_{model}=5±1, 50 % N_{model}=8±1 yielded a fit mean of 6.5 and residual of 0.15. For N_{Lig}=12 (Fig. 5c), 30 % N_{model}=4±1, 70 % N_{model}=9±1 yielded a fit mean of 7.5 and residual of 0.12. The fact that multimodal models fit the data best reiterates the fact that stochastic reaction processes are taking place during the synthesis of the HRP-AuNPs and yields a distribution of HRP:AuNP ratios within the product with a given mean and standard deviation [18].

From data analysis of the quantitative immunostaining AFM images, it is possible to calculate the reaction yields, represented as the fit mean divided by N_{Lig}. The reaction yields are reasonably comparable to those predicted by solution stoichiometry, ranging from 62 % to 93 %. The overall trend of the data in Figs. 3 and 4 suggests increasing the amount of ligand in the reaction increases the final ligand loading on the particle. This illustrates the types of studies that are enabled by this approach; however, more datasets should be collected before such a trend can be confidently applied to broader situations based on the data reported in this work.

The quantitative immunostaining by AFM technique's true strength lies in its ability to resolve quantitatively the number of ligands on single NPs, while providing a metric to compare with the integrative techniques with the fit mean value. The refined models presented in this work provide higher confidence when interpreting quantitative results, especially in regards to assessing the NP to NP heterogeneity of number of ligands actually bound to the NP surface. Multimodal distribution models provided a better fit than any broad mono-modal distribution could for all but one of the example datasets collected in this work. This novel measurement approach confirms there is clearly a heterogeneity in the distribution of observed N_{Lig} values and that this heterogeneity is likely greater than previously assumed.

Conclusion

A refined probabilistic model has been developed, to improve the quantitative interpretation of immunostaining results when assaying for the number of biomolecules conjugated to a NP surface. Key assumptions from previous models and additional new assumptions to account for steric constraints and system geometries were combined into this new model. Sample data sets were analyzed with this new model and found to agree reasonably well with expected solution chemistry reaction yields. Comparisons to previous models and datasets revealed that this new model can provide quantitative results closer to solution stoichiometries.

Future work should explore even more subtle details of the statistical calculations. For example, it is more physically realistic to assign coordinates for each surface Au atom that could serve as the bonding atom for a ligand molecule. Additionally, assigning a binding probability coefficient factor, ranging from 0 for completely blocked Au atoms up to 1 for Au atoms far enough away that no repulsive forces between ligands (electrostatic, steric, or otherwise) will be present, would enable a more "fine-grained" approach that was found to be too computationally intensive for the routine desktop PC user implementation proposed here. Access to greater computational resources employing fine-grained approaches could provide useful reference curves for the field that would only need to be calculated one time and model even more physically realistic situations occurring on NP surfaces.

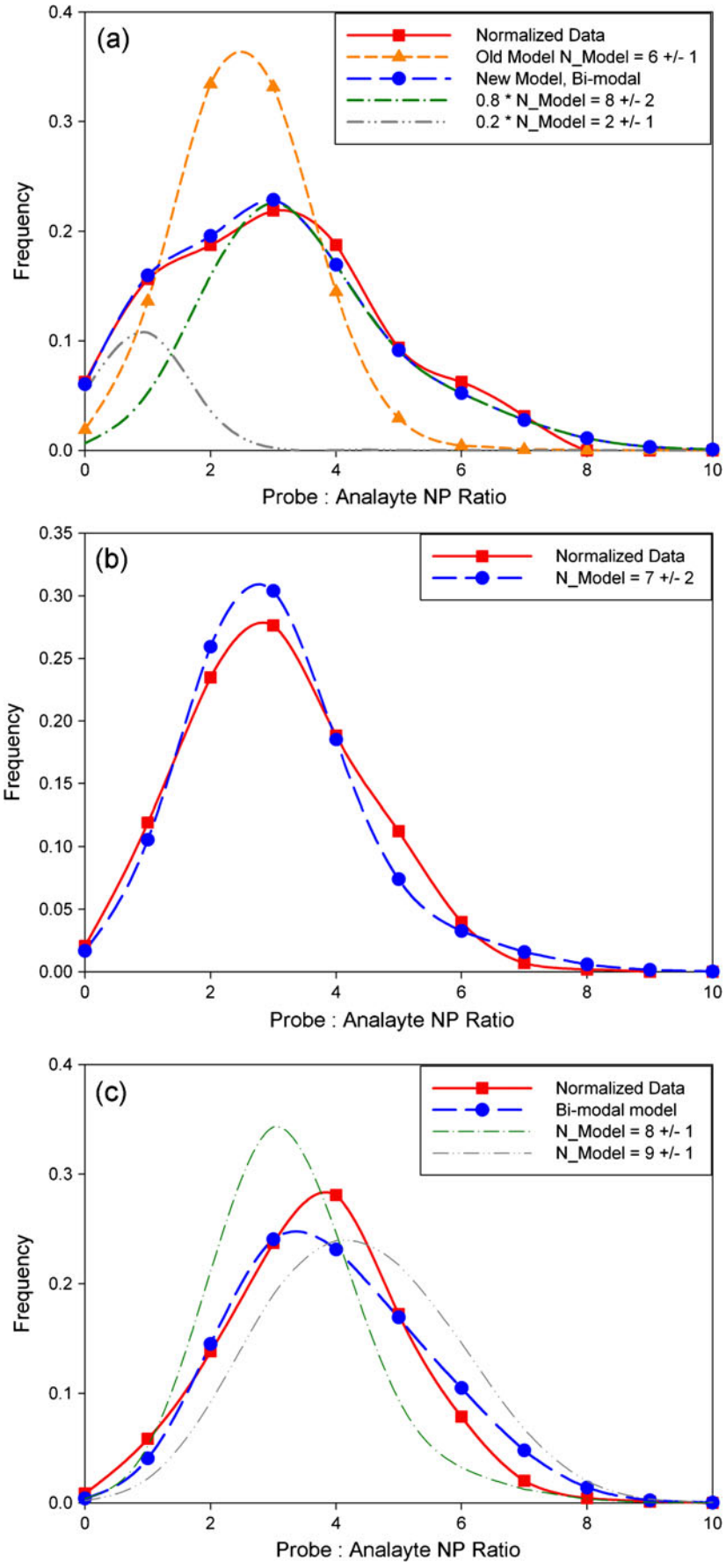

Fig. 4 **a** Previously reported 60 nm Au analtye NPs with N_{Lig}=10 data (*squares*) and model (*triangles*) (Geronimo et al. [26]) and new model (*circles*) using bi-modal distribution of 80 % N_{model}=8±2, 20 % N_{model}=2±1. Fit mean=6.8. Residual of old model=0.52, residual of new model=0.07. **b** 30 nm Au analyte NP with N_{Lig}=10 HRP, batch #1, observed normalized data, and model fit. N_{model}=7±2, residual=0.13. **c** 30 nm Au analyte NP with N_{Lig}=10 HRP, batch #2. Fit is bi-modal distribution, 30 % N_{model}=7±1, 70 % N_{model}=9±1. Fit mean=8.4, residual=0.15. *Dashed lines* show N_{model}=8±1and N_{model}=9±1models to illustrate utility of bi-modal models

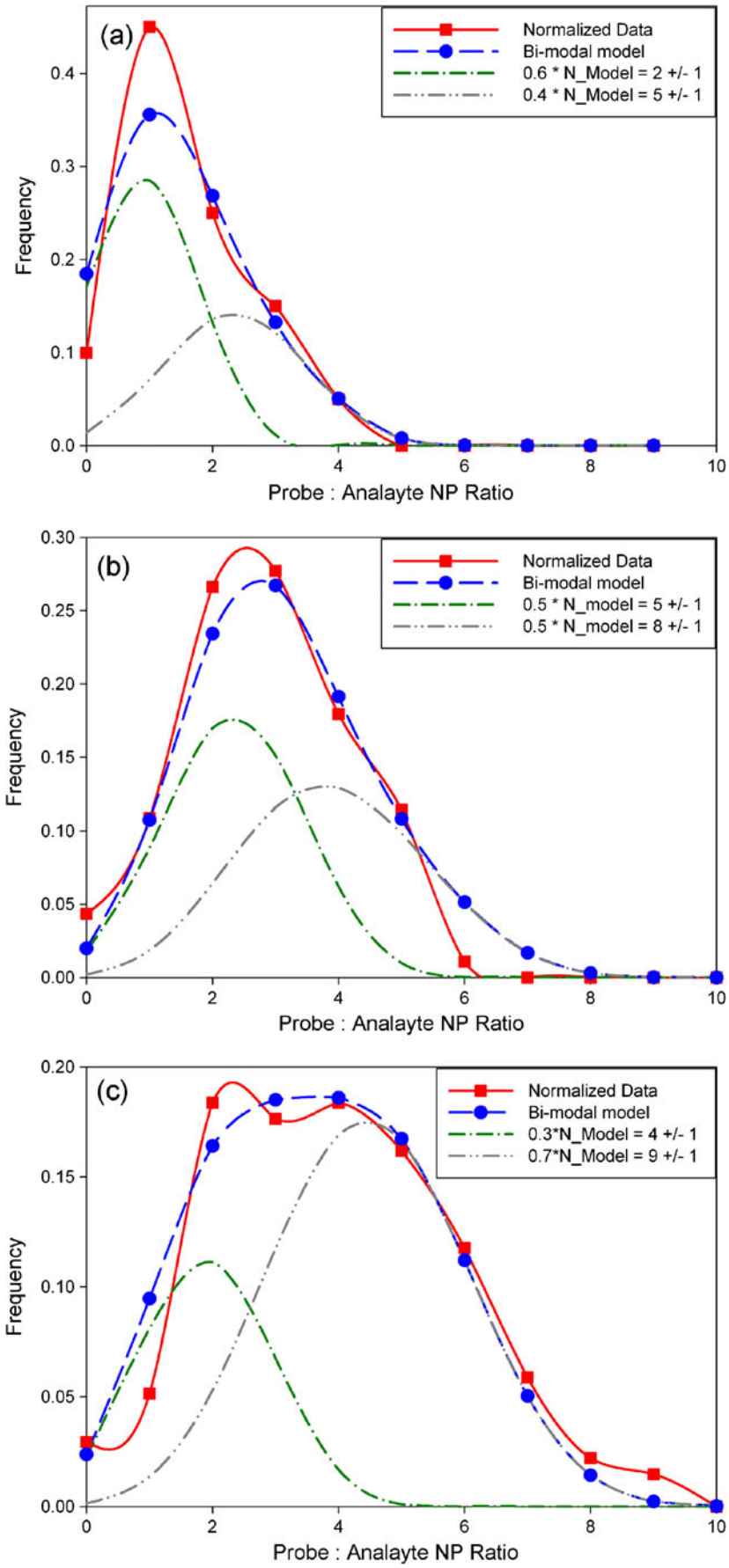

Fig. 5 The 60-nm Au analyte NPs with HRP and bi-modal distribution fits. **a** N_{Lig}=5. Fit is 60 % N_{model}=2±1, 40 % N_{model}=5±1. Fit mean=3.2, residual=0.22. **b** N_{Lig}=7. Fit is 50 % N_{model}=5±1, 50 % N_{model}=8±1. Fit mean=6.5, residual=0.15. **c** N_{Lig}=12. Fit is 30 % N_{model}=4±1, 70 % N_{model}=9±1. Fit mean=7.5, residual=0.12

Acknowledgments The authors thank Drs. Julian Taurozzi, Laura Espinal, Joshua Martin, Chris Forrey, and Richard Gates for insightful discussion and helpful comments preparing this manuscript.

References

1. Daniel MC, Astruc D (2004) Gold nanoparticles: assembly, supramolecular chemistry, quantum-size-related properties, and applications toward biology, catalysis, and nanotechnology. Chem Rev 104:293–346
2. Eck W, Craig G, Sigdel A, Ritter G, Old LJ, Tang L, Brennan MF, Allen PJ, Mason MD (2008) PEGylated gold nanoparticles conjugated to monoclonal F19 antibodies as targeted labeling agents for human pancreatic carcinoma tissue. ACS Nano 2:2263–2272
3. Paciotti GF, Myer L, Weinreich D, Goia D, Pavel N, McLaughlin RE, Tamarkin L (2004) Colloidal gold: a novel nanoparticle vector for tumor directed drug delivery. Drug Deliv 11:169–183. doi:10.1080/10717540490433895
4. Crist RM, Grossman JH, Patri AK, Stern ST, Dobrovolskaia MA, Adiseshaiah PP, Clogston JD, McNeil SE (2012) Common pitfalls in nanotechnology: lessons learned from NCI's Nanotechnology Characterization Laboratory. Integr Biol
5. Marquis B, Maurer-Jones M, Lin YS, Ersin M, Haynes C (2011) The bench scientist's perspective on the unique considerations in nanoparticle regulation. J Nanopart Res 1–12
6. Hall JB, Dobrovolskaia MA, Patri AK, Mcneil SE (2007) Characterization of nanoparticles for therapeutics. Nanomedicine 2:789–803
7. McNeil SE (2009) Nanoparticle therapeutics: a personal perspective. WIREs Nanomed Nanobiotechnol 1:264–271. doi:10.1002/wnan.6
8. Elghanian R, Storhoff JJ, Mucic RC, Letsinger RL, Mirkin CA (1997) Selective colorimetric detection of polynucleotides based on the distance-dependent optical properties of gold nanoparticles. Science 277:1078–1081
9. Elzey S, Tsai DH, Rabb S, Yu L, Winchester M, Hackley V (2012) Quantification of ligand packing density on gold nanoparticles using ICP-OES. Anal Bioanal Chem 403:145–149
10. Tsai DH, Shelton MP, DelRio FW, Elzey S, Guha S, Zachariah MR, Hackley VA (2012) Quantifying dithiothreitol displacement of functional ligands from gold nanoparticles. Anal Bioanal Chem 404:3015–3023
11. Elzey S, Tsai DH, Yu LL, Winchester MR, Kelley ME, Hackley VA (2013) Real-time size discrimination and elemental analysis of gold nanoparticles using ES-DMA coupled to ICP-MS. Anal Bioanal Chem 405:2279–2288
12. Zook JM, Long SE, Cleveland D, Geronimo CLA, MacCuspie RI (2011) Measuring silver nanoparticle dissolution in complex biological and environmental matrices using UV-visible absorbance. Anal Bioanal Chem 401:1993–2002. doi:10.1007/s00216-011-5266-y
13. Cho TJ, Zangmeister RA, MacCuspie RI, Patri AK, Hackley VA (2011) Newkome type dendron stabilized gold nanoparticles: syntheses, reactivity, and stability. Chem Mater 23:2665–2676. doi:10.1021/cm200591h
14. Tsai D-H, Davila-Morris M, Delrio FW, Guha S, Zachariah MR, Hackley VA (2011) Quantitative determination of competitive molecular adsorption on gold nanoparticles using attenuated total reflectance-Fourier transform infrared spectroscopy. Langmuir 27:9302–9313. doi: 10.1021/la2005425
15. Jespersen ML, Mirau PA, Meerwall E, Vaia RA, Rodriguez R, Giannelis EP (2010) Canopy dynamics in nanoscale ionic materials. ACS Nano 4:3735–3742. doi:10.1021/nn100112h
16. Woehrle GH, Brown LO, Hutchison JE (2005) Thiol-functionalized, 1.5-nm gold nanoparticles through ligand exchange reactions: scope and mechanism of ligand exchange. J Am Chem Soc 127:2172–2183
17. Slocik JM and Naik RR (2010) Probing peptide-nanomaterial interactions. Chem Soc Rev 39:3454-3463
18. Levy R, Wang ZX, Duchesne L, Doty RC, Cooper AI, Brust M, Fernig DG (2006) A generic approach to monofunctionalized protein-like gold nanoparticles based on immobilized metal ion affinity chromatography. Chembiochem 7:592–594. doi:10.1002/cbic.200500457
19. Sevick-Muraca EM, Houston JP, Gurfinkel M (2002) Fluorescence-enhanced, near infrared diagnostic imaging with contrast agents. Curr Opin Chem Biol 6:642–650
20. Szollosi J, Damjanovich S, Matyus L (1998) Application of fluorescence resonance energy transfer in the clinical laboratory: routine and research. Cytometry 34:159–179
21. Jain KK (2003) Nanodiagnostics: application of nanotechnology in molecular diagnostics. Expert Rev Mol Diagn 3:153–161
22. Maeshima K, Eltsov M, Laemmli UK (2005) Chromosome structure: improved immunolabeling for electron microscopy. Chromosoma 114:365–375
23. Yezhelyev MV, Gao X, Xing Y, Al-Hajj A, Nie SM, O'Regan RM (2006) Emerging use of nanoparticles in diagnosis and treatment of breast cancer. Lancet Oncol 7:657–667
24. Achilefu S (2004) Lighting up tumors with receptor-specific optical molecular probes. Technol Cancer Res Treat 3:393–409
25. Romer T, Leonhardt H, Rothbauer U (2011) Engineering antibodies and proteins for molecular in vivo imaging. Curr Opin Biotechnol 22:882–887
26. Geronimo CLA, MacCuspie RI (2011) Antibody-mediated self-limiting self-assembly for quantitative analysis of nanoparticle surfaces by atomic force microscopy. Microsc Microanal 17:206–214. doi:10.1017/S1431927610094559
27. El Rifai OM, Youcef-Toumi K (2004) On automating atomic force microscopes: an adaptive control approach. Decision and Control, 43rd IEEE Conference , vol 2, 1574–1579
28. Neffati R, Alexeev A, Saunin S, Brokken-Zijp JCM, Wouters D, Schmatloch S, Schubert US, Loos J (2003) Automated scanning probe microscopy as a new tool for combinatorial polymer research: conductive carbon black/poly(dimethylsiloxane) composites. Macromol Rapid Comm 24:113–117
29. Boyd R, Cuenat A (2011) New analysis procedure for fast and reliable size measurement of nanoparticles from atomic force microscopy images. J Nanopart Res 13:105–113. doi:10.1007/s11051-010-0007-2
30. Fischbarg, J (1978) Fluid transport by corneal epithelium. In: Schmidt-Nielsen, Bolis, and Maddrell (ed) Comparative Physiology: Water, ions, and fluid mechanics. Cambridge, UK, Cambridge University Press 21–21
31. Striemer CC, Gaborski TR, McGrath JL, Fauchet PM (2007) Charge- and size-based separation of macromolecules using ultrathin silicon membranes. Nature 445:749–753. doi:10.1038/nature05532
32. MacCuspie RI, Banerjee IA, Pejoux C, Gummalla S, Mostowski HS, Krause PR, Matsui H (2008) Virus assay using antibody-functionalized peptide nanotubes. Soft Matter 4:833–839. doi:10.1039/b714470a
33. Domingos RF, Baalousha MA, Ju-Nam Y, Reid MM, Tufenkji N, Lead JR, Leppard GG, Wilkinson KJ (2009) Characterizing manufactured nanoparticles in the environment: multimethod determination of particle sizes. Environ Sci Technol 43:7277–7284
34. MacCuspie RI (2011) Colloidal stability of silver nanoparticles with various surface coatings in biologically relevant conditions. J Nanopart Res 13:2893–2908. doi:10.1007/s11051-010-0178-x
35. Li X, Lenhart JJ, Walker HW (2011) Aggregation kinetics and dissolution of coated silver nanoparticles. Langmuir 28:1095–1104. doi:10.1021/la202328n
36. MacCuspie RI, Rogers K, Patra M, Suo Z, Allen AJ, Martin MN, Hackley VA (2011) Challenges for physical characterization of silver nanoparticles under pristine and environmentally relevant conditions. J Environ Monit 13:1212–1226. doi:10.1039/c1em10024f
37. Romer I, White TA, Baalousha M, Chipman K, Viant MR, Lead JR (2011) Aggregation and dispersion of silver nanoparticles in exposure media for aquatic toxicity tests. J Chromatogr A 1218:4226–4233. doi:10.1016/j.chroma.2011.03.034